Recognition of Articulated Objects in SAR Images

Bir Bhanu, Grinnell Jones, Joon Ahn, Ming Li, and **June Yi**
College of Engineering
University of California
Riverside, California 92521

Abstract

We are investigating hierarchical approaches for indexing/matching of articulated targets in SAR images using pseudo-invariants, symmetry, persistence and uniqueness of scatterers based on physical reasoning and topographical primal sketch features. This paper presents our initial model-based approaches for target signature modeling, indexing and matching. We describe a method that efficiently retrieves correct object hypotheses using the major axis of a pattern of scattering centers in SAR images and the Hausdorff distance measure. The features that we use here are the locations of scattering centers. We show results on XPATCH generated data for T-72, T-80 and FRED tanks, and SCUD missile launcher in articulated positions with and without occlusion.

1 Introduction

Our focus for automatic target recognition (ATR) now is on synthetic aperture radar (SAR) sensors in support of matching/indexing for the moving and stationary target acquisition and recognition (MSTAR) program. This and the accompanying papers [14, 31] describe the progress in the areas of automatic model construction from ISAR images, image segmentation and recognition of articulated targets in SAR images.

Our goal is to develop physically-based approaches having multiple representations for indexing and matching to recognize articulated targets in SAR images. The key features of our approach to recognizing a large number of articulated targets are: (a) use models for articulation, (b) use physics-based modeling to relate features with target geometry, (c) use polymorphic features based on their stability, persistence and uniqueness, (d) combine many features with templates for hypothesis and verification.

*This work is supported by grants MDA972-93-1-0010 and DAAH049510448. The contents of the paper do not necessarily reflect the position or the policy of the U.S. Government.

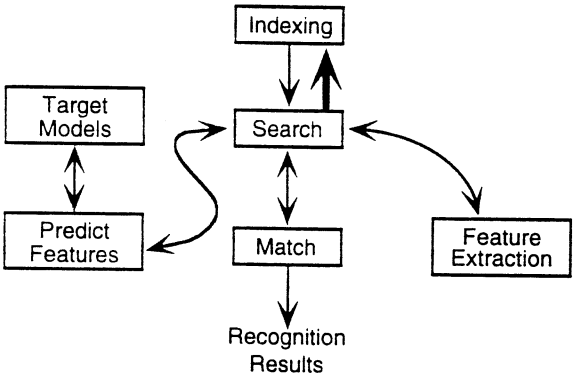

Figure 1: Part of the MSTAR architecture for model-based target recognition in SAR images. The arrow shown in bold is not a part of the architecture.

and (e) construct models for indexing and matching automatically. We also allow interaction between search and indexing modules unlike the prediction, feature extraction, match and search (PEMS) components of the MSTAR architecture (see Figure 1). It enables us to consider hierarchical and incremental approaches that give SEARCH and MATCH more control, rather than a take-it-or-leave-it approach [20].

Recognition of articulated objects in SAR images is a challenging problem. A simple approach may consider each of the articulated parts of an object as separate objects. However, such an approach is quite inefficient since it will require a large model database. Moreover, it may not be effective in distinguishing targets from different classes. We want to develop an efficient recognition approach that inherently models the articulated nature of an object such as a SCUD missile launcher or a tank with different positions of turret and gun.

ATR from SAR imagery is an important aspect of

current vision research. Some of the representative work in ATR from SAR images includes [13] [21] and [28]. This work focuses on template matching techniques in which the templates are manually designed. However, few research works on target indexing using SAR images have been published in the literature. Indexing is one of the fundamental issues in model-based recognition that is concerned with how accurately and efficiently the process can narrow down the number of candidate models to be matched without actually searching through all the models in a database. This research features accurate and efficient target indexing in SAR images given locations of scattering centers.

We have developed a computationally simple approach that efficiently retrieves correct model hypotheses when objects are represented by a pattern of point features. In the indexing table, model entries are indexed with the major axes of the patterns of scattering centers. We first index the input pattern of scattering centers using its major axis and validate candidate hypotheses using the Hausdorff distance measure.

Our matching approach based on topographic primal sketch (TPS) and other features is under development where we use hierarchical decision trees to select various features based on the amount of information gain, confidence in the feature and the kind of surface from which a feature may originate.

We have done extensive experimentation with XPATCH to generate articulated models for T-72, T-80, M1a1 tanks and a SCUD launcher at various azimuth and depression angles . We have done interactive analysis in relating the persistent scatters with the target geometry and we have developed programs to generate the model automatically [31]. We have evaluated the performance of our initial approach to indexing and matching with respect to scaling, occlusion, articulation, and occlusion with articulation. The results are very good when there is no occlusion and begin to deteriorate in the presence of occlusion and articulation, especially with articulation.

2 Target Signature Modeling and Scene Generation

The XPATCH radar signature prediction code [2] and the XPATCH_ES ground-mapping radar sensor simulation code were used to simulate the radar signature of vehicle targets and ground scenes. The XPATCH code predicts the radar signature of targets that are represented by computer aided design (CAD) descriptions of geometry and materials contained in facet files. CAD models of tanks (including the T-72, T-80 and M1a1) and a SCUD Missile Launcher were used. Target materials were assumed to be perfectly electrically conducting, except for the tires of the SCUD Launcher which were coded to represent radar transparent material. Articulated target models were constructed by editing the facet files to rotate the tank turrets to various angles and to erect the SCUD Missile on the launch stand. Target signatures were generated at "six inch" resolution in X-band (maximum frequency 10.5 GHZ, a 1.0 GHZ frequency bandwidth and a 5.6° angular span) to be comparable with the resolution of the University Research Initiative (URI) Synthetic Dataset. Results were obtained for all target azimuths from 0° to 359° in 1° steps at a 15° depression angle. In addition, two foot resolution target chips, required for the XPATCH_ES ground scene simulations, were generated in X-band (maximum frequency of 10.12 GHZ. a 0.25 GHZ frequency bandwidth and a 1.4° angular span).

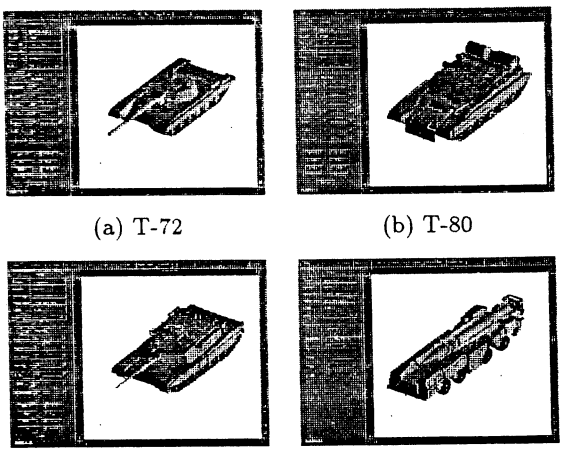

(a) T-72 (b) T-80

(c) M1a1 (d) SCUD

Figure 2: T-72, T-80, M1a1 and SCUD Launcher targets.

Target geometries of some non-articulated target models (T-72, T-80, M1a1 and SCUD Launcher) are shown in Figure 2. Example signatures for the T-72 at 70°, 210°, 290° and 330° are shown in Figure 3, where the azimuth angle is measured clockwise from the vehicle forward longitudinal centerline to the incoming SAR direction (in from the left of the page in the SAR image Figures). For the tanks, at "six inch" resolution, the individual track wheels tend to show up as a row of bright returns near the leading edge. For the T-72 tank model, the strongest returns are typically from trihedral corners on the rear upper deck of the tank hull. Example signatures for the SCUD Launcher at 70° and 142° are shown in Figure 4. The returns are typically from features on the up-range side of the vehicle, because the missile usually hides the view of much of the down-range side.

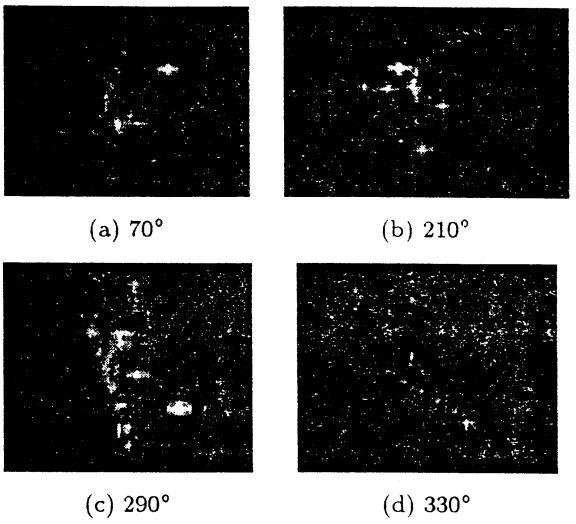

(a) 70° (b) 210°

(c) 290° (d) 330°

Figure 3: T-72 (0° turret) signatures.

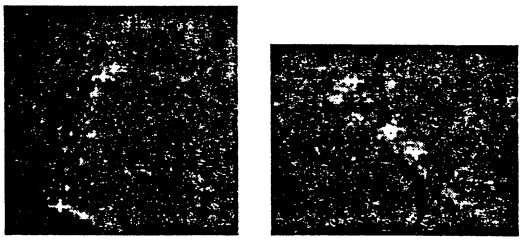

(a) 70° (b) 142°

Figure 4: SCUD Launcher (missile down) signatures.

Target geometries of some articulated target models, T-72 tank with a 60° turret (counterclockwise angle from the hull forward centerline to the main gun axis) and the SCUD Launcher with the missile erected on the launch stand, are shown in Figure 5. Example signatures of the T-72 (with 60° turret) at azimuths of 70°, 210°, 290° and 300° are shown in Figure 6. The front views, 0° azimuth, of the T-72 in Figure 9 (with a 0° turret on the left, 60° on the right) illustrate that rotation of the turret can shadow regions of the hull (compare returns in the lower right quadrants in Figure 9) and also introduce variations in the return from areas corresponding to the turret and main gun. Example signatures of the SCUD Launcher at azimuths of 70° and 142° with the missile erect on the launch stand are shown in Figure 10. The missile itself can be seen near the top of both views in Figure 10 and with the missile up out of the way, many areas on the down-range side of the vehicle are now visible.

Test simulations of SAR ground mapping imagery were generated using the XPATCH_ES code with

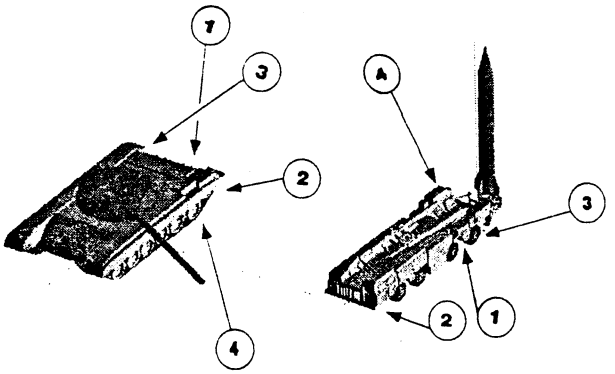

Figure 5: T-72 (60° turret) and SCUD Launcher (missile erect) targets.

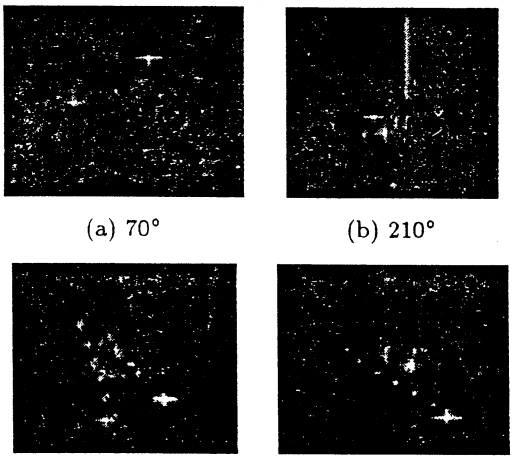

(a) 70° (b) 210°

(c) 290° (d) 330°

Figure 6: T-72 (60° turret) signatures.

two foot resolution T-72 tank target signature chips produced by XPATCH. An example image, at 15° depression angle, is shown in Figure 7 with seven T-72 tank targets, grass, trees, a road and a wire fence. The SAR direction is from the top of the image, with the shadows extending downward. The target locations in the scene can be seen in Figure 8 where the tanks are located within the circles. The orientation of the 7 tanks are: top row — 0°, second row down (hidden in the tree shadow — 30°, third row — 180°, and the four tanks in the bottom row are from left to right — 60°, 90°, 120°, and 150°.

3 Indexing

In indexing, the feature correspondence and search of model database are replaced by a table look-up

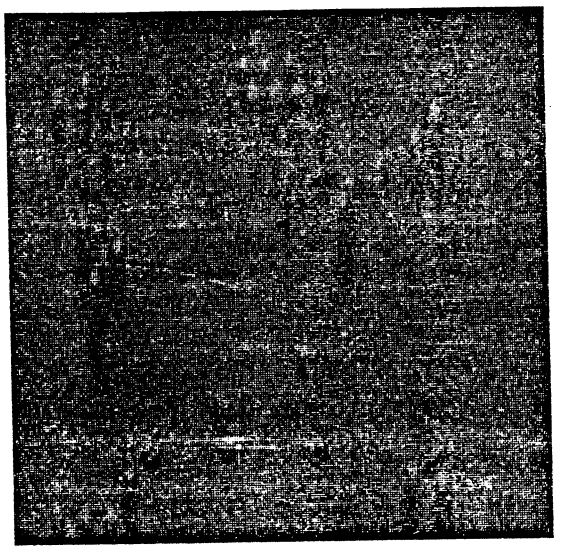

Figure 7: Simulated SAR scene with T-72 tanks.

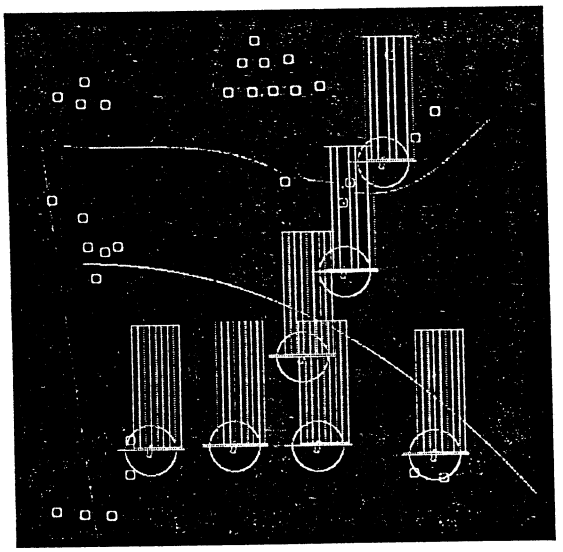

Figure 8: Target locations in simulated SAR scene.

mechanism. This indexing table is computed off-line. A brief survey of some representative object recognition systems that have employed geometric indexing or hashing techniques is given in Table 1. Performance of these systems cannot be compared directly because they have been developed based on different assumptions. They perform in different scenarios using different features to generate object hypotheses. More importantly, it is hard to compute complex structured features from point-like features that SAR returns although those approaches marked with asterisk (*) in Table 1 are potentially applicable to the problem of ATR from SAR images.

A block diagram of our preliminary object recognition system is given in Figure 11. The entire system is divided into two parts: off-line simulation of SAR

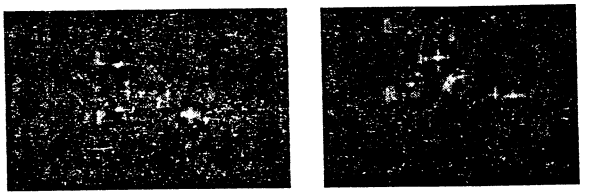

(a) 0° turret (b) 60° turret

Figure 9: T-72 (0° and 60° turret) signatures at 0° azimuth.

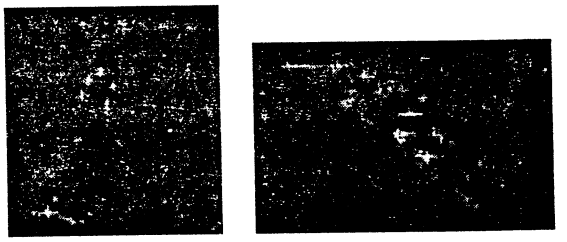

(a) 70° (b) 142°

Figure 10: SCUD Launcher (missile erect) signatures.

signatures of model objects and construction of indexing table and on-line recognition. In the off-line part, SAR images of target models represented by CAD files are simulated with the XPATCH software for a set of aspects (represented by *depression* and *azimuth* angles). For each image, locations of scattering centers are detected and its direction of major axis is computed. In the indexing table, model hypotheses represented by (*model name, depression angle, azimuth angle, location of scattering centers*) are linked to indexing keys that are directions of their major axes. At recognition time, scattering centers are extracted from the target chip. The major axis of the pattern of scattering centers is computed and models whose major axis is within $\pm\epsilon^\circ$ (threshold) neighborhood of the input major axis are quickly collected from the indexing table. At this stage, we apply the Hausdorff distance measure to match the scattering centers of the models and the target chip so as to validate the candidate hypotheses. We rank-order these hypotheses and they enter the verification stage in the order they are listed.

3.1 Computing Major Axis

We employed the principal component analysis to compute the major axis of a pattern of scattering centers. The use of this technique is specialized to two dimensions in this work, however, it can be used with input data of any dimensionality.

Assume that the input data is expressed as a matrix

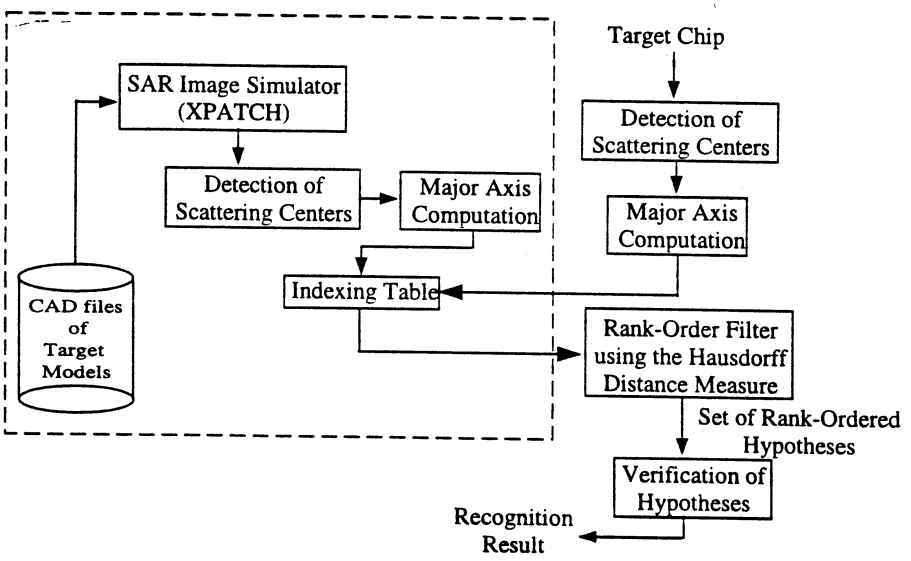

Figure 11: System Overview

Table 1: State-of-the-art techniques for indexing.

system	acquisition /recognition input data	indexing key
Yi and Chelberg [30]	3D/3D range image	Local Surface Group
Califano and Mohan [9]	2D/2D 2D drawing	seven dimensional global invariants
* Rigoutsos and Hummel [22]	2D/2D intensity image	coordinates of scene points computed in the coordinate system formed by an ordered pair of scene points
Beis and Lowe [4]	2D/3D range image	three angles and ratio of the interior edge lengths from four straight-line segment chain
Stein and Medioni [24]	2D/2D intensity image	super segments with several different cardinalities for edges
Stein and Medioni [25]	3D/3D range image	3D super segments with several different cardinalities for edges and splashes
Flynn and Jain [15]	3D/3D range image	two invariant feature values computed from a triple of scene surface patches that are simultaneously visible
* Lamina et al.	2D/2D intensity image	coordinates of scene points in the affine-transformed coordinate system formed by an ordered triplet of three scene points

$\mathbf{X}$ with each row i containing the coordinates of one of the scattering centers $\mathbf{x}_i = (x_i, y_i)$:

$$\mathbf{X} = \begin{bmatrix} x_1 & y_1 \\ \vdots & \\ x_n & y_n \end{bmatrix}.$$

The following steps are performed using this input matrix:

1. The sample mean is computed for x and y coordinates as $\hat{\mu}_x = (1/n)\sum_{i=1}^{n} x_i$ and $\hat{\mu}_y = (1/n)\sum_{i=1}^{n} y_i$, respectively. A centered data matrix $\mathbf{X}^*$ is constructed from $\mathbf{X}$:

$$\mathbf{X}^* = \begin{bmatrix} x_1 - \hat{\mu}_x & y_1 - \hat{\mu}_y \\ \vdots & \\ x_n - \hat{\mu}_x & y_n - \hat{\mu}_y \end{bmatrix}.$$

2. The sample covariance matrix $\hat{\mathbf{R}} = 1/n[\mathbf{X}^*]^t\mathbf{X}^*$ is obtained and its eigensystem is computed, yielding two eigenvalue and eigenvector pairs $\{(\mathbf{v}_1, \lambda_1), (\mathbf{v}_2, \lambda_2)\}$, such that the two pairs are sorted so that $\lambda_1 \geq \lambda_2$.

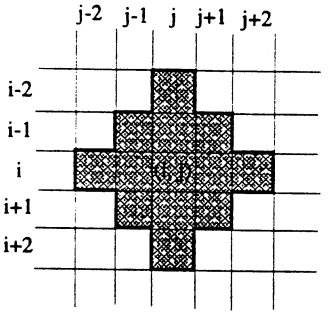

Figure 12: Local neighborhood (filled region) that is used to detect scattering centers.

The two eigenvectors, $\mathbf{v}_1$ and $\mathbf{v}_2$, span the 2D imaging plane and the eigenvector $\mathbf{v}_1$ is the direction in the plane along which the data's sample variance is the larger (λ_1 is the sample variance along the direction $\mathbf{v}_1$). $\mathbf{v}_2$ is the direction orthogonal to $\mathbf{v}_1$ with the larger variance. The directionality of $\mathbf{v}_i$ is an excellent estimate of the orientation of scattering pattern. To resolve the 180° ambiguity, we use the direction that forms an acute angle with x axis as the direction of major axis.

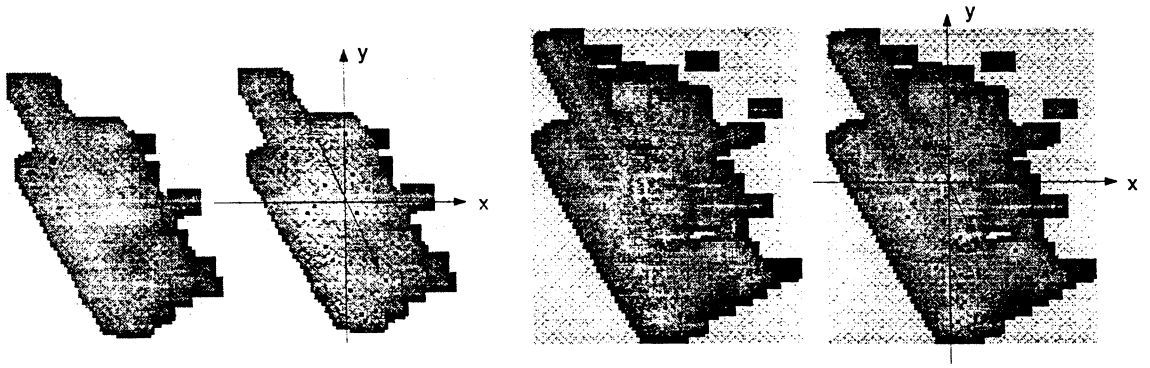

(a) FRED tank (b) T72 tank

Figure 13: Magnitude of SAR returns (left) and scattering centers marked with small dark squares (right) for (a) FRED tank (b) T72 tank at azimuth angle 60° and elevation angle 15°. Only target region is taken from 256x256 target chip and zoomed in for clear visualization of scattering centers in the target. The original sizes of images in (a) and (b) are 62x78 and 78x93, respectively.

3.2 The Hausdorff Distance Measure

Given two finite point sets $A = \{a_1, \cdots, a_p\}$ and $B = \{b_1, \cdots, b_q\}$, the Hausdorff distance is defined as

$$H(A, B) = \max(h(A, B), h(B, A))$$

where

$$h(A, B) = \max_{a \in A} \min_{b \in B} \|a - b\|$$

and $\|\cdot\|$ is some underlying norm on the points of A and B. The function $h(A, B)$ is called the *directed* Hausdorff distance from A to B. It identifies the point $a \in A$ that is farthest from any point of B and measures distance from a to its nearest neighbor in B (using the given norm $\|\cdot\|$), that is, $h(A, B)$ in effect ranks each point of A based on its distance to the nearest point of B and then uses the largest ranked such point as the distance (the most mismatched point of A). Point of A must be within distance d of some points of B, and also there is some point of A that is exactly distance d from the nearest point of B (the most mismatched point). The Hausdorff distance $H(A, B)$ is the maximum of $h(A, B)$ and $h(B, A)$. Thus, it measures the degree of mismatch between two sets by measuring the distance of the point of A that is farthest point of any point of B and vice versa. The notion of resemblance encoded by this distance measure is that each member of A be near some member of B and vice versa. Unlike most methods of comparing shapes, there is no explicit pairing of points of A with points of B (for example, many points of A may be close to the same point of B). The function $H(A, B)$ can be trivially computed in time $O(pq)$ for two point sets of size p and q, respectively, and this can be improved to $O((p+q)\log(p+q))$ [1].

3.3 Experimental Results for Indexing

In the first part of experiment, the model database includes two armored vehicle targets, FRED tank (a generic tank data set supplied with XPATCH software) and T72 tank. The radar signature predictions (at six inch resolution for all azimuths from 0° to 359° in 1° steps at 15° elevation) of these tanks are generated using the XPATCH SAR simulation code.

We employ the following method to detect scattering centers. Other, more complicated, methods can be used, as long as they produce locations of scattering centers. We consider current pixel location a candidate scattering center if the magnitude of SAR return at the current pixel is a local maximum in the local neighborhood shown in Figure 12. Current pixel location is considered a local maximum if the following four conditions are met.

$$z(i,j-2) < z(i,j-1) < z(i,j) > z(i,j+1) > z(i,j+2)$$
and
$$z(i-2,j) < z(i-1,j) < z(i,j) > z(i+1,j) > z(i+2,j)$$
and
$$z(i-1,j-1) < z(i,j) > z(i+1,j+1)$$
and
$$z(i-1,j+1) < z(i,j) > z(i+1,j-1),$$

where $z(i, j)$ represents the magnitude of the image at the current pixel location, (i, j). The same method is used for detection of scattering centers at both off-line and on-line processes. Examples of scattering centers detected using this method and major axes computed from these scattering centers are shown in Figure 13 for FRED tank and T72 tank at azimuth angle 60°. Top twenty scattering centers in terms of magnitude are selected in this experiment. If the number of scattering centers is less than twenty, all available scattering centers are

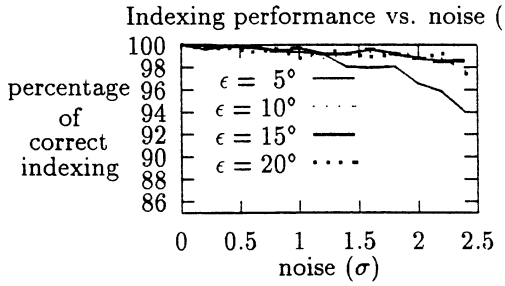

Figure 14: Indexing performance of the algorithm as the amount of positional noise varies.

used. After all scattering centers are identified, indexing table is built where a model entry, (*model name, depression angle, azimuth angle, locations of scattering centers*), is linked to a leaf node of binary tree that spans a small range (ϵ) of directions containing the major axis direction of the entry. For experiment, data for all azimuth angles from 0° to 359° are used as test data. We generate noisy locations of scattering centers, $(x + N_1(0, \sigma^2), y + N_2(0, \sigma^2))$, using two Gaussian random noise generators, N_1 and N_2. (x, y) is a noiseless location of a scattering center and $N(0, \sigma^2)$ denotes Gaussian noise of mean, 0, and standard deviation, σ in units of pixels. We have employed a rather strict requirement for a successful indexing. We consider an indexing result correct only when the first model entry ordered by the Hausdorff distance measure is the same as the input. Figure 14 shows the indexing performance of our method as the amount of positional noise added to location of scattering centers varies. Even though the amount of noise increases, the accuracy of indexing does not degrade significantly. As expected, the result shows that we need to use larger value of $\epsilon°$ to retrieve model hypotheses when noise gets large.

3.3.1 Scaling, Occlusion and Articulation Experiments

After experimenting with two objects FRED tank and T72 tank, we added T80 tank and SCUD missile launcher into the model database. Thus, we have a total of four model classes in the database. Based on this model database, we performed four experiments. Figure 15 shows the indexing performance. Note that performance is quite good for scaling and partial occlusion. However, as expected for our global approach based on Hausdorff measure, it deteriorates magnitude with articulation and occlusion.

4 Matching

Table 3 shows the summary of techniques used for recognition of articulated objects. Table 2 shows the summary of techniques used for recognition of objects in SAR images.

Table 2: A summary of techniques for recognition of objects in SAR images

Researchers	Technique	Object
Chang & Lu [10]	MSF	Car/Van/Pick-up
Cruthirds *et al.* [12]	BCS & FCS	Landscape
Novak *et al.* [21]	Template Correlation	Tanks
Sato *et al.* [23]	Deformable Template Matching	Planes
Verly *et al.* [27]	Functional Template Correlation	Tank/Truck/APC
Waxman *et al.* [28]	NN & Aspect Graph	Tanks
Wong & Posner [29]	Scale-Space Clustering	Landscape

4.1 Feature Extraction

4.1.1 Local Maxima

Observing local maxima of an intensity image is a simple way of analyzing the characteristics of the image. Building the model database with local maxima will reduce the space for storage and time for comparison. Here we have employed a simple method of detecting local maxima. The method is based on comparing the pixel value with its immediate eight neighbors. If the current pixel value is greater than all the other immediate eight neighbors, then it is a local maximum. We extracted the top forty local maxima from the images of SCUD missile launcher and T72 tank. In the captions of Figure 16(a) through 17(d), SCUD means that the missile is down on the launcher and SCUP means that the missile is up. In the captions of Figure 18(a) through 19(d), T7200 means that the turret of T72 tank is straight forward and T7260 means that the turret of T72 tank is rotated 60° with respect to the body. In all captions of Figure 16(a) through 19(d), the three digit numbers represent the aspect angles of the objects.

4.1.2 SCUD missile launcher

SCUD missile launcher has two poses of articulation, the one with the missile down and the other with

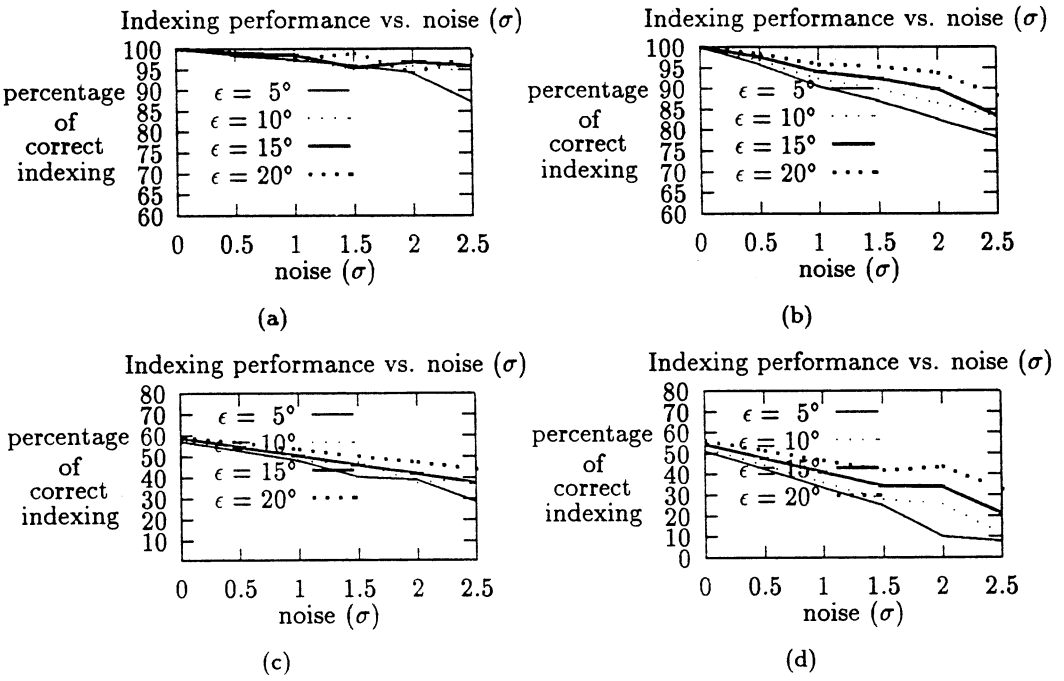

Figure 15: Indexing performance of the algorithm for four targets, Fredtank, T72 tank, T80 tank, and SCUD missile launcher with missile in the down position. (a) Scaling experiment. (b) 10% occlusion for all four targets. (c) Same as (a) but the turret of tank T72 is articulated by 60° for each aspect. (d) Same as (c) but with 10% occlusion for T72 target for all 360 aspects.

the missile up. Figure 16(a), 17(a) and 17(b) are the XPATCH SAR images of SCUD missile launcher with the missile down at aspect angles 0°, 60°, and 120°, respectively. Figure 16(b), 17(c) and 17(d) are the SAR images of SCUD missile launcher with the missile up at aspect angles 0°, 60°, and 120°, respectively. All Figures have small black dots at the position of local maxima.

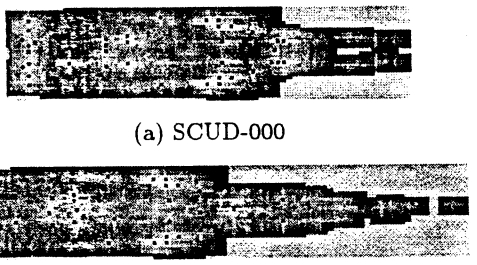

(a) SCUD-000

(b) SCUP-000

Figure 16: SCUD missile launcher

4.1.3 T72 Tank

For the T72 tank, two poses of articulation were used, one with the turret aligned with the body and the other with the turret rotated 60° with respect to the body. Figure 18(a), 19(a) and 19(b) are the XPATCH SAR images of T72 tank with the turret straight at aspect angles 0°, 60°, and 120°, respectively. Figure 18(a), 19(a) and 19(b) are the XPATCH SAR images of T72 tank with the turret rotated 60° at aspect angles 0°, 60°, and 120°, respectively. All Figures have small black dots at the position of local maxima.

4.1.4 Discussion

For Figures 16(a) through 19(d), the radar is directed from the left direction. From each image, we extracted the top forty local maxima.

Figure 16(a) and Figure 16(b) show that many of the local maxima don't change whether the missile is up or down. Figure 16(a) shows more local maxima around the missile stand which is located at the back side of the launcher. When the missile is up, the missile stand does not give strong return. But the image is longer compared to the one when the missile is down because there is a longer path for multiple bounce between the launcher body and missile body.

Figure 17(a) and Figure 17(c) show another characteristic. Most of the local maxima form a narrow L shape in the missile down image (Figure 17(a)), while they form a wider, well spread out local maxima in the missile up image (Figure 17(c)).

Table 3: Summary of techniques used for recognition of articulated objects

Techniques Authors	Principles of the Technique	Results	Applicability to SAR images
Recognition by Components *Biederman* [7]	Recognize each component as an arrangement of geons. Recognize whole object by relationship among components	Objects are recognized quickly if an arrangement of two or three geons can be recovered from the image	Extraction of geons from SAR images may not be possible
Generalized Hough Transform *Beinglass & Wolfson* [3]	Use transformation invariant shape signature to calculate the index of R-table. Pick the rotary joint position as the reference center. Check the high scoring candidates if there are only two high scoring.	Object considerably occluded can be recognized by accumulating scores from each component connected by joint. Components not linked by a joint does not contribute to recognize the object.	Detection of the joint and interesting feature must be reliable in SAR image
Context-Based Vision *Worrall et al.* [26]	Extract the contours of objects. Obtain the best local pose starting from a seed pose by searching for a local optimum of the evaluation function.	A direct approach towards pose refinement is demonstrated. Deformable model improves the performance of pose refinement by allowing the use of additional contextual knowledge.	Extraction of the contours may be possible from SAR image
Framework for Recognition and Localization *Hel-Or & Werman* [18]	Define models using a set of constraints that describe the natural relationship between the components. Obtain the measurement of a constrained object. Using the Kalman filter, estimate the pose by fusion of the actual measurements and the uncertainties.	The functional dependency includes only the local parameters. Can deal with all types of constraints including inequalities.	In SAR images, the correspondence of feature parts to various parts is nontrivial.

In some aspect angles, 120° for example, the missile up position is clearly recognized. In general, missile up images are wider than missile down images.

Similar analysis can be done for the T72 tank images. Strong returns are along the body of the tank which can be used for hypothesizing aspect angle. In Figure 18(a) and Figure 18(b), there are consistent returns on the front of the tank and the back right side. If we separate the images into two parts, one for body and one for turret, then we can see the similarity between the bodies with the same angle (Figure 19(a) and Figure 19(c), Figure 19(b) and Figure 19(d)). Also, we can see the similarity between the turrets with the same angle (Figure 19(a) and Figure 18(b), Figure 19(b) and Figure 19(c)).

4.2 Experiments and Results for Matching

Figures 21 through 22 show the results of experiments for the recognition of articulated objects in SAR images with occlusion. There are three steps in the experiment: indexing, 2D Hausdorff distance measurement and 1D Hausdorff distance measurement. We used two kind of models, FRED tank and T72 tank. T72 tank has the turret rotated 0°, 60° and 90°.

In the indexing stage, we estimate the orientation of the target and use the result as the indexing value to narrow down the search space of the matching hypothesis. We set the angle tolerance from 5° to 20° with 5° steps. In Figures 21 and 23, the *index* lines show the successful indexing results. We consider the indexing is successful if the matching hypothesis is in the result of indexing.

In the 2D Hausdorff distance measurement, we used *directed* Hausdorff distance measurement $h(A, B)$ where A is the point feature of a testing image and B is the point feature of a database. The reason that we used the *directed* Hausdorff distance measurement ($h(A, B)$) instead of the Hausdorff distance measurement ($H(A, B)$) is to make the algorithm

(a) SCUD-060 (b) SCUD-120

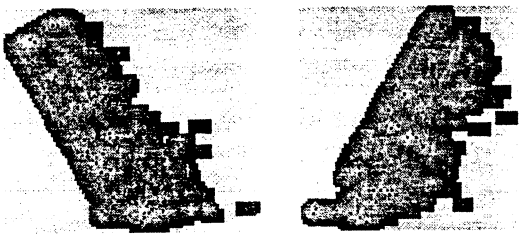

(c) SCUP-060 (d) SCUP-120

Figure 17: SCUD missile launcher

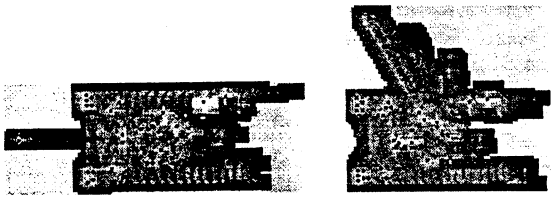

(a) T7200-000 (b) T7260-000

Figure 18: T72 tank

(a) T7200-060 (b) T7200-120

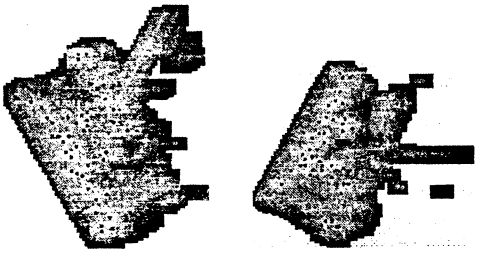

(c) T7260-060 (d) T7260-120

Figure 19: T72 tank

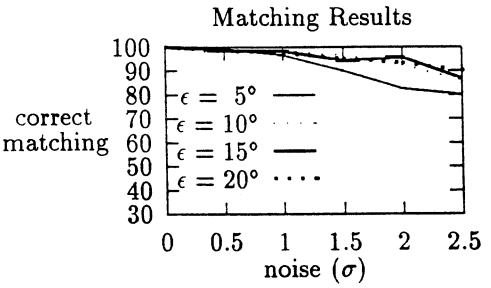

Figure 20: Matching results without Occlusion

work for occluded images. We assume occlusion of the target occured and part of the target return is not observed in the input image. In the Figures 21 and 23 the *first* lines show the successful matching after the 2D *directed* Hausdorff distance measurement.

In the 1D Hausdorff distance measurement, we used the magnitudes of the SAR returns in dB. We calculated the dB differences from the highest peak value to every other peak and enumerated the differences in increasing order. Then we used them as the input of the *directed* 1D Hausdorff measurement. In Figures 21 and 23 the *final* lines show the final matching results using 1D and 2D *directed* Hausdorff distance measurement.

The Figure 20 shows the experimental result for the data without occlusion, and the Figure 22 shows the results for the data with occlusion. We generated the occlusion data by removing 15% of points from the input image. In 5° angle variation, the indexing results with occlusion are less than 50% correct . As the angle variation increases, the indexing results are increased up to 90% which is still less than non-occluded cases. In both occluded and non-occluded cases the matching improves by using the 1D Hausdorff distance measurement.

5 Other Features

5.1 Topographic Primal Sketch (TPS)

According to differential geometry, local surface shape is uniquely determined by the first and second fundamental forms [6]. Gaussian and mean curvature combine these first and second fundamental forms in two different ways to obtain scalar surface features that are invariant to rotation, translation, and changes in parameterization [5]. Also, mean curvature uniquely determines the shape of graph

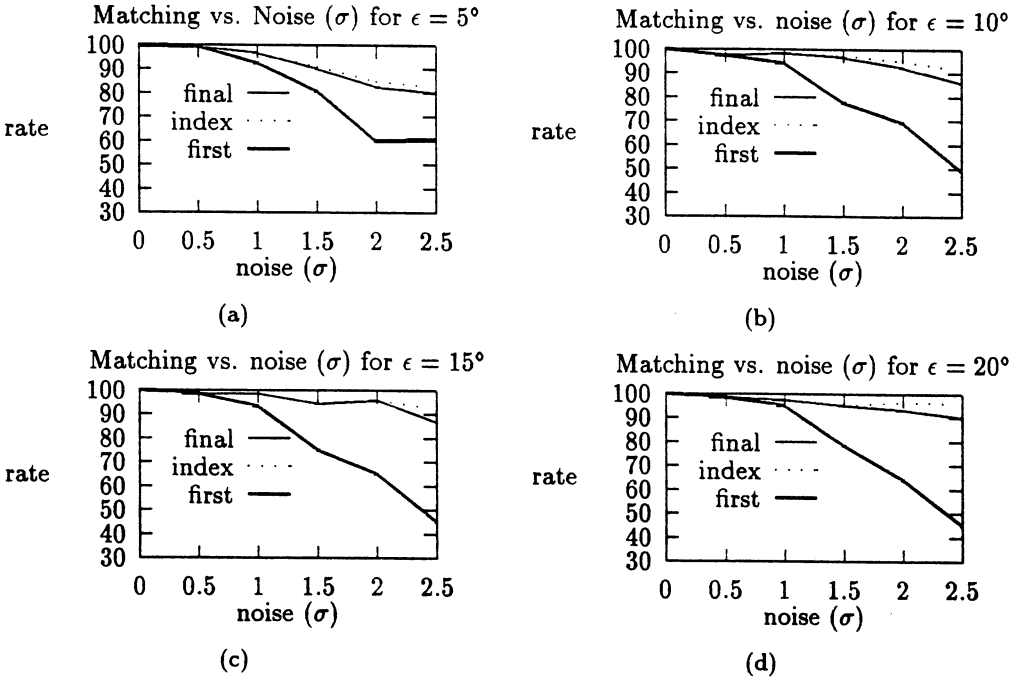

Figure 21: Matching vs. noise without Occlusion

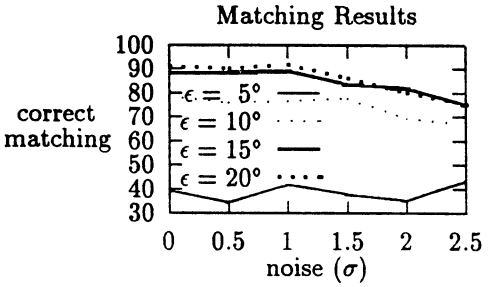

Figure 22: Matching results with Occlusion

surfaces if a boundary curve is also specified [16] while Gaussian curvature uniquely determines the shape of convex surfaces and convex regions of non-convex surfaces [11], [19]. There are eight fundamental viewpoint independent surface types that can be characterized using only the sign of the mean curvature (H) and Gaussian curvature (K) as shown in Table 4 [6].

A program that classifies each image pixel into eight categories (peak, pit, ridge, valley, flat, saddle, saddle ridge, saddle valley) has been developed. This program uses two curvatures, Gaussian curvature and mean curvature. Based on the sign of the two curvatures on a given pixel of image, that pixel will be classified into one of the eight categories.

The algorithm that creates a surface type label image $\mathbf{T}(i,j)$ from the original image $\mathbf{g}(i,j)$ in the following manner:

Table 4: Surface type labels from surface curvature sign.

	$K > 0$	$K = 0$	$K < 0$
$H < 0$	Peak	Ridge	Saddle Ridge
$H = 0$	(none)	Flat	Minimal Surface
$H > 0$	Pit	Valley	Saddle Valley

- Compute partial derivative images $\mathbf{g}_u(i,j)$, $\mathbf{g}_v(i,j)$, $\mathbf{g}_{uu}(i,j)$, $\mathbf{g}_{vv}(i,j)$, $\mathbf{g}_{uv}(i,j)$ from the original image $\mathbf{g}(i,j)$ using local fixed-window surface fits that are accomplished via convolution operators.
- Using the partial derivative images, compute the mean curvature image $\mathbf{H}(\mathbf{g}_u, \mathbf{g}_v, \mathbf{g}_{uu}, \mathbf{g}_{vv}, \mathbf{g}_{uv})$ and the Gaussian curvature image $\mathbf{K}(\mathbf{g}_u, \mathbf{g}_v, \mathbf{g}_{uu}, \mathbf{g}_{vv}, \mathbf{g}_{uv})$.
- Compute the sign $(+,-,0)$ of mean curvature, denoted by sgn (H), and the sign of Gaussian curvature, denoted by sgn (K). The signum function sgn (x) maps negative numbers to -1, positive numbers to $+1$, and zero maps to 0.
- Use surface curvature sign to determine a surface type label $\mathbf{T}(i,j)$ for each pixel (i,j).

The equations of Gaussian curvature (K) and mean

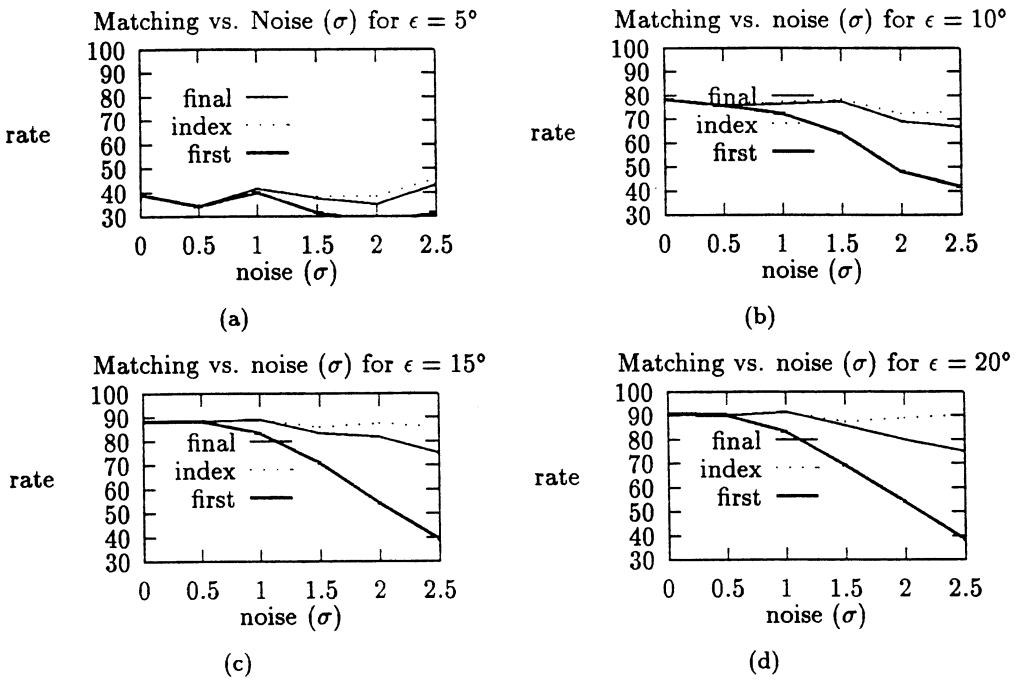

Figure 23: Matching vs. noise with Occlusion

curvature (H) are given below.

$$\mathbf{X}(i,j) = (1 + \mathbf{g}_v^2(i,j))\mathbf{g}_{uu}(i,j)$$

$$\mathbf{Y}(i,j) = (1 + \mathbf{g}_u^2(i,j))\mathbf{g}_{vv}(i,j)$$

$$\mathbf{Z}(i,j) = \mathbf{g}_u(i,j)\mathbf{g}_v(i,j)$$

$$\mathbf{H}(i,j) = \frac{\mathbf{X}(i,j)+\mathbf{Y}(i,j)-2\mathbf{Z}(i,j)}{2(\sqrt{1+\mathbf{g}_u^2(i,j)+\mathbf{g}_v^2(i,j)})^3}$$

$$\mathbf{K}(i,j) = \frac{\mathbf{g}_{uu}(i,j)\mathbf{g}_{vv}(i,j)+\mathbf{g}_{uv}^2(i,j)}{(1+\mathbf{g}_u^2(i,j)+\mathbf{g}_v^2(i,j))^2}$$

Figure 24 (a) through (h) show the eight topographic primal sketch features [17]for the T72 tank at azimuth angle 60°.

5.2 Persistence of Scattering Centers and Symmetry

For the T-72 tank model, the strongest returns that are often persistent for 20° of azimuth (or more) are typically from trihedral corners on the rear upper deck of the tank hull (labeled 1 through 4 in Figure 5. The persistence of these corners for turret angles of 0° and 60° can be seen from Table 5 where the angular span is the range of azimuths for which the return from that location is the peak signature from the target.

The SCUD Launcher model is basically a mirror image about the longitudinal centerline and the returns

Table 5: Angular span of T-72 persistent scattering centers.

corner	turret 0	turret 60
1	62 - 83	61 - 82
2	187 - 224	190 - 256
3	278 - 298	279 - 297
4	299 - 357	298 - 355

for various azimuths are largely symmetric about 180°. Four areas of persistent scattering centers are labeled 1 through 4 in the SCUD Launcher view of Figure 5 (their mirror image locations are also scattering centers). The fourth scattering center, located on the down-range side of the vehicle is only active when the missile is moved up out of the way. The persistence of these scattering centers, in terms of azimuth angle span, for the SCUD Launcher with the missile in both the down and the up positions is given in Table 6. The centers labeled M4 through M1 are the mirror image locations of 1 through 4. The centers labeled 4a and 4b are the same physical location which is the strongest return for two angular spans.

In our learning-from-examples approach [31] for automatic struction of recognition models from ISAR data, we have also used the persistence of scatterers. A novel feature of the approach is that it uses the persistence of scattering centers computed during training phase to extract good scattering centers

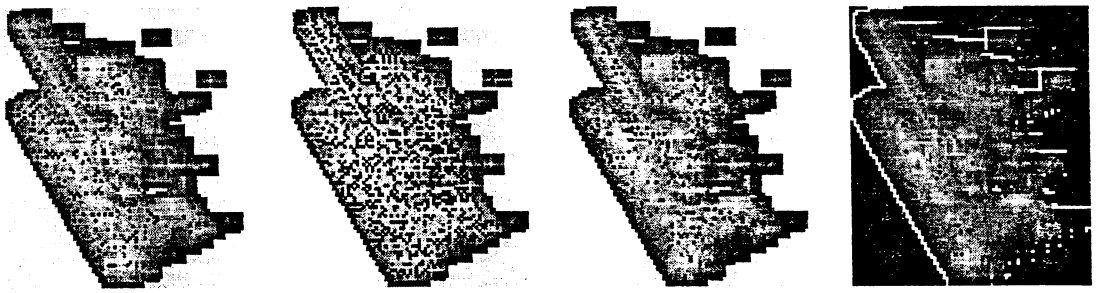

(a) Pit (b) Valley (c) Saddle Valley (d) Flat

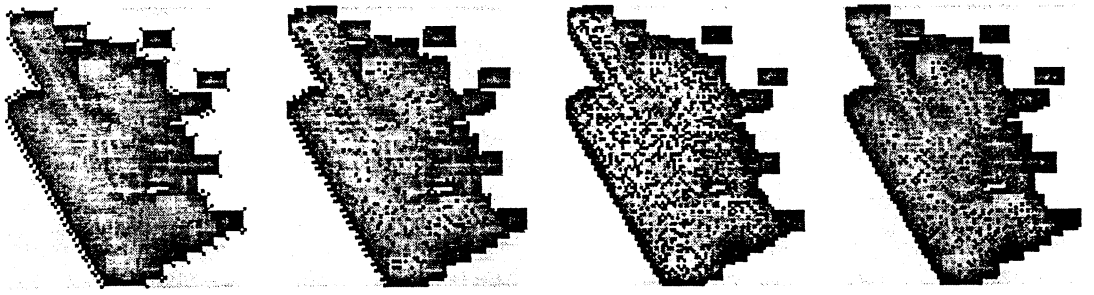

(e) Minimal (f) Saddle Ridge (g) Ridge (h) Peak

Figure 24: Topographic Primal Sketch features for T72 tank with aspect 60°

Table 6: Angular span of SCUD Launcher persistent scattering centers.

center	missile down	missile up
1	16 - 51	12 - 48
2	59 - 83	59 - 82
4a	(none)	114 - 141
3	126 - 155	142 - 155
4b	(none)	156 - 165
M4b	(none)	195 - 204
M3	205 - 234	205 - 215
M4a	(none)	219 - 248
M2	277 - 301	278 - 301
M1	309 - 345	307 - 345

during testing phase.

6 Conclusions

In this paper, we have presented our initial researches for indexing and matching. Our goal is to develop physically-based approaches having multiple representations for indexing and matching to recognize articulated targets in SAR images. We will develop hierarchical matching algorithms that detect the aspect of the object and recognize the model and articulation. We will study the characteristics of TPS on SAR images. We will evaluate the complete system with respect to scaling, occlusion, articulation, and occlusion with articulation. we are also developing an approach for indexing that is based on hidden Markov models [8]. Currently the experiments with SAR imagery are in progress with this approach.

References

[1] E. Alt, B. Behrends, and J. Blomer. Measuring the resemblance of polygonal shapes. In *Proceedings of the Seventh ACM Symposium on Computational Geometry*, 1991.

[2] D. J. Andersh, S. W. Lee, H. Ling, and C. L. Yu. Xpatch: A high frequency electromagnetic scattering prediction code using shooting and bouncing ray. In *Proceedings of Ground Target Modeling and Validation Conference*, pages 498–507, August 1994.

[3] A. Beinglass and H. J. Wolfson. Articulated object recognition, or : How to generalize the generalized hough transform. In *Conf. on Computer Vision and Pattern Recognition*, June 1991.

[4] J. Beis and D. Lowe. Learning indexing functions for 3-D model-based object recognition. In *Conf. on Computer Vision and Pattern Recognition*, pages 275–280, June 1994.

[5] P. J. Besl. Surfaces in early range image understanding. *Ph.D. dissertation, Dep. Elec. Eng. Comput. Sci., Univ. Michigan, Ann Arbor, Rep. RSD-TR-10-86*, March 1986.

[6] P. J. Besl and R. C. Jain. Segmentation through variable-order surface fitting. In *IEEE Trans. Pattern Analysis and Machine Intelligence*, March 1988.

[7] I. Biederman. Recognition-by-components: A theory of human image understanding. *Psychology Review 94*, 1987.

[8] W. Burger and B. Bhanu. Signal-to-symbol conversion for structural object recognition using hidden Markov models. In *Proc. ARPA Image Understanding Workshop*, pages 1287–1291, Monterey, California, November 14-16 1994.

[9] A. Califano and R. Mohan. Multidimensional indexing for recognizing visual shapes. *IEEE Trans. Pattern Analysis and Machine Intelligence*, 6(4):373–392, April 1994.

[10] K. C. Chang and Y. C. Lu. Feedback learning: a hybrid sofm/lvm approach for radar target classification. *Proceedings of 1994 International Symposium on Artificial Neural Networks*, pages 465–470, December 1994.

[11] S. S. Chern. A proof of the uniqueness of minkowski's problem for convex surfaces. In *Amer. J. Math.*, volume 79, pages 949–950, 1957.

[12] D. Cruthirds, A. Gove, S. Grossberg, E. Mingolla, N. Nowak, and J. Williamson. Processing of synthetic aperture radar images by the boundary contour system and feature contour system. *International Joint Conference on Neural Networks*, 4:414–419, 1992.

[13] D. E. Dudgeon, R. J. Lacoss, C. H. Lazott, and J. G. Verly. Use of persistent scatterers for model-based recognition. In *Proceedings of SPIE Conference on Algorithms for Synthetic Aperture Radar Imagery*, volume 2230, pages 356–368, Orlando, FL, April 1994.

[14] T. A. Ferryman and B. Bhanu. A Bayesian approach for the segmentation of SAR images using dynamically selected neighborhoods. In *Proc. ARPA Image Understanding Workshop*, Palm Springs, California, February 13-16 1996.

[15] P. Flynn and A. K. Jain. 3D object recognition using invariant feature indexing of interpretation tables. In *Proceedings of the first IEEE CAD-Based Workshop*, pages 115–123, June 1991.

[16] D. Gilbarg and N. Trudinger. Elliptic partial differential equations of second order. *Berlin:Springer-Verlag*, 1983.

[17] R. M. Haralick and L. G. Shapiro. Computer and robot vision. *Abbison-wesley publishing company*, volume 1, 1992.

[18] Y. Hel-Or and M. Werman. Recognition and localization of articulated objects. In *AO*, 1992.

[19] B. K. P. Horn. Extended Gaussian images. In *Conf. on Computer Vision and Pattern Recognition*, pages 1656–1678, December 1984.

[20] R. Hummel. Private communication relating to MSTAR. 1995.

[21] L. M. Novak, G. J. Owirka, and C. M. Netishen. Performance of a high-resolution polarimetric SAR automatic target recognition system. *The Lincoln Laboratory Journal*, 6(1):11–24, 1993.

[22] I. Rigoutsos and R. Hummel. Distributed Bayesian object recognition. In *Conf. on Computer Vision and Pattern Recognition*, pages 180–186, June 1993.

[23] K. Sato, K. Ikeuchi, and T. Kanade. Model based recognition of specular objects using sensor models. *Computer Vision, Graphics, and Image Processing: Image Understanding*, 55(2):155–169, March 1992.

[24] F. Stein and G. Medioni. Structural indexing: Efficient 2-D object recognition. *IEEE Trans. Pattern Analysis and Machine Intelligence*, 14(12):1198–1204, December 1992.

[25] F. Stein and G. Medioni. Structural indexing: Efficient 3-D object recognition. *IEEE Trans. Pattern Analysis and Machine Intelligence*, 14(2):125–145, February 1992.

[26] G. D. Sullivan, A. D. Worrall, and J. M. Ferryman. Visual object recognition using deformable models of vehicles. In *CBV*, June 1995.

[27] J. Verly, R. Delanoy, and C. Lazott. Prociples and evaluation of an automatic target recognition system for synthetic aperture radar imagery based on the use of functional templates. In *SPIE proceedings on automatic target recognition III*, pages 1–15, April 1993.

[28] A. M. Waxman, M. Seibert, A. M. Bernardon, and D. A. Fay. Neural systems for automatic target learning and recognition. *The Lincoln Laboratory Journal*, 6(1):77–116, 1993.

[29] Y. Wong and E. C. Posner. A new clustering algorithm applicable to multispectral and polarimetricsar images. *IEEE Transactions on Geoscience and Remote Sensing*, 31(3):634–644, May 1993.

[30] J. H. Yi and D. M. Chelberg. Rapid obeject recognition from a large model database. In *Proceedings of the second IEEE CAD-Based Workshop*, pages 28–35, 1994.

[31] S. Zhang and B. Bhanu. Automatic model construction for object recognition using inverse synthetic aperture radar images. In *Proc. ARPA Image Understanding Workshop*, Palm Springs, California, February 13-16 1996.

1996 Proceedings

Image Understanding Workshop — Vol. II

Palm Springs Hilton
12 - 15 February
Palm Springs, California

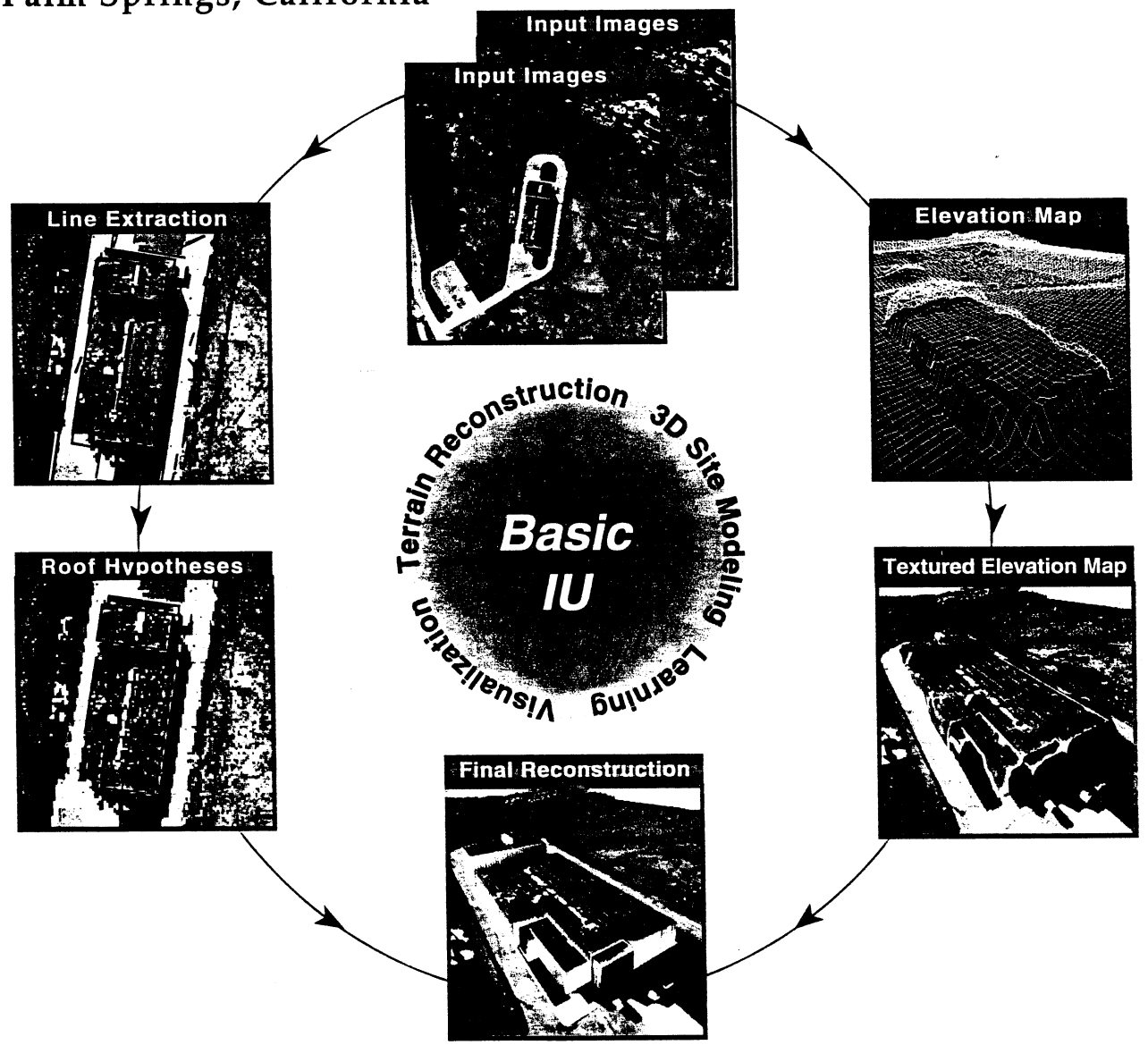

The cover is provided by the
Image Understanding Research Program at the
University of Massachusetts

Sponsored by:

Advanced Research Projects Agency
Information Systems Office
Image Understanding Program

IMAGE UNDERSTANDING WORKSHOP

Proceedings of a Workshop
held in
Palm Springs, California

February 12 - 15, 1996

Volume II

Sponsored by:
Advanced Research Projects Agency
Information Systems Office

This document contains copies of reports prepared for the ARPA Image Understanding Workhsop. Included are Principal Investigator reports and technical results from both the basic and strategic computing programs within ARPA/ISO sponsored projects and certain technical reports from selected scientists from other organizations.